



Upper mantle seismic anisotropy as a constraint for mantle flow and continental dynamics of the North American plate



Wanying Wang^{a,b,*}, Thorsten W. Becker^{a,b}

^a Institute for Geophysics, Jackson School of Geosciences, University of Texas at Austin, Austin, TX, USA

^b Department of Geological Sciences, Jackson School of Geosciences, University of Texas at Austin, Austin, TX, USA

ARTICLE INFO

Article history:

Received 21 November 2018

Received in revised form 28 February 2019

Accepted 11 March 2019

Available online xxxx

Editor: R. Bendick

Keywords:

continental dynamics

seismic anisotropy

North American plate

ABSTRACT

The alignment of intrinsically anisotropic olivine crystals under convection is typically invoked as the cause of the bulk of seismic anisotropy inferred from shear-wave splitting (SWS). This provides a means of constraining the interplay between continental dynamics and the deep mantle, in particular for densely instrumented regions such as North America after USArray. There, a comparison of “fast orientations” from SWS with absolute plate motions (APM) suggests that anisotropy is mainly controlled by plate motions. However, large regional misfits and the limited realism of the APM model motivate us to further explore SWS based anisotropy. If SWS is estimated from olivine alignment in mantle circulation instead, plate-driven flow alone produces anisotropy that has large misfits with SWS. The addition of large-scale mantle density anomalies and lateral viscosity variations significantly improves models. Although a strong continental craton is essential, varying its geometry does, however, not improve the plate-scale misfit. Moreover, models based on higher resolution tomography degrade the fit, indicating issues with the flow model assumptions and/or a missing contributions to anisotropy. We thus compute a “lithospheric complement” to achieve a best-fit, joint representation of asthenospheric and frozen-in lithospheric anisotropy. The complement shows coherent structure and regional correlation with independently imaged crustal and upper mantle anisotropy. Dense SWS measurements therefore provide information on depth-dependent anisotropy with implications for tectonics, but much remains to be understood about continental anisotropy and its origin.

© 2019 Elsevier B.V. All rights reserved.

1. Introduction

Upper mantle seismic anisotropy is suggested to be mainly caused by the alignment of olivine aggregates in mantle flow. This is referred to as olivine lattice preferred orientation (LPO), and LPO is expected to align with shear under convection. This relationship provides a link between asthenospheric flow and seismic observations, in particular to study the relationships between surface geology and the underlying mantle dynamics in continental plates (e.g. Silver, 1996; Long and Becker, 2010). In order to obtain information about upper mantle flow, shear-wave splitting (SWS) analysis of teleseismic phases is widely used to infer azimuthal anisotropy. SWS measures the separation of shear waves into two orthogonally polarized pulses upon traversing an anisotropic medium. The polarization plane orientation of the faster shear wave pulse is often called the “fast azimuth”, and is expected to parallel the alignment

of the seismically fast [100]-axes of the olivine aggregates and the sense of shear. The delay time between the fast and slow wave arrivals at the surface indicates the anisotropy magnitude accumulated along the path, and by inference, the depth extent or layer thickness of the anisotropic part of the mantle or lithosphere (e.g. Silver, 1996; Savage, 1999). Teleseismic SWS measurements use SKS, SKKS and PKS phases that have nearly vertical ray paths and sample the upper mantle beneath the seismic stations with poor vertical, but good lateral resolution.

Recently, the USArray seismometer deployment during the EarthScope effort provided unprecedented coverage of United States, renewing efforts to investigate mantle dynamics within and underneath the North American plate (e.g. Hongsresawat et al., 2015; Long et al., 2016; Zhou et al., 2018). Here, we compare a range of mantle flow model predictions of upper mantle anisotropy to the observed SWS fast orientations to advance our understanding of North America upper mantle dynamics (Fig. 1).

The SWS dataset used in this study is shown in Fig. 1b and newly spans the whole continent at roughly uniform station spacing. The SWS compilation consists of 14,326 splits from the updated compilation of Becker et al. (2012), as well 29,061 stan-

* Corresponding author at: Institute for Geophysics, Jackson School of Geosciences, University of Texas at Austin, Austin, TX, USA.

E-mail address: wanying@utexas.edu (W. Wang).

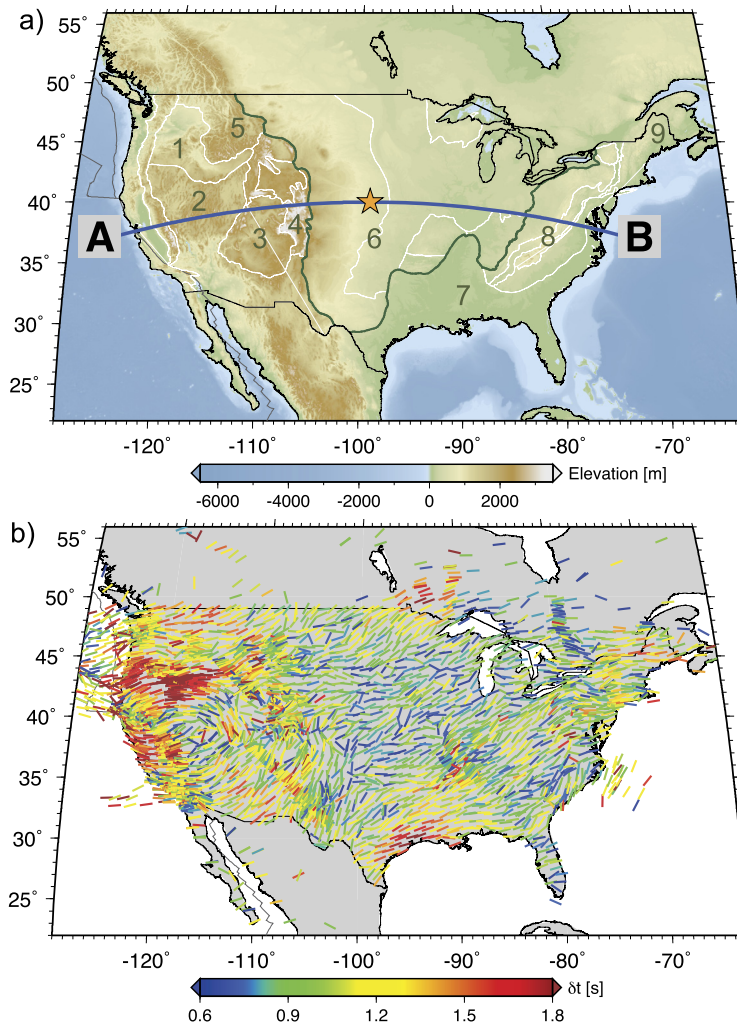


Fig. 1. Study area showing topography and physio-geographic regions (a) and station-averaged shear-wave splitting measurements (b). In a), elevation is shown in the background; green lines are the orographic boundaries here used to define the western, central and eastern U.S.; white lines are the boundaries of different physio-geographic regions; blue profile shows the location of the cross section of the flow profiles discussed below. Main physio-geographic regions that are discussed in this paper are marked with numbers, they are: 1) Columbia Plateau, 2) Basin and Range, 3) Colorado Plateau, 4) Southern Rocky Mountains, 5) Northern Rocky Mountains, 6) Interior Plains, 7) Coastal Plains, 8) Appalachian Mountain Range, and 9) New England province. In b), fast orientation and delay times (δt) of the SWS measurement compilation are shown by stick orientation and color, respectively. (For interpretation of the colors in the figure(s), the reader is referred to the web version of this article.)

standardized splits from Liu et al. (2014), Refayee et al. (2014), and Yang et al. (2016, 2017). We also include results from offshore experiments (Bodmer et al., 2015; Ramsay et al., 2015; Lynner and Bodmer, 2017).

As has been discussed earlier based on more limited compilations, the fast SWS orientation within the U.S. are generally E-W to NW-SE (e.g. Silver, 1996), exhibit a circular pattern beneath the Great Basin (e.g. Zandt and Humphreys, 2008; Hongsresawat et al., 2015), and orogen-parallel orientation beneath and around the Appalachians (e.g. Long et al., 2016) (Fig. 1b). While we mainly consider fast azimuths below, we note that the delay times of SWS vary in systematic fashion. Broadly speaking, delay times are larger beneath most of the western U.S. and the south central U.S., and smaller beneath the interior plain, the Appalachians and the southern Great Basin (Fig. 1b).

In order to link those observations of azimuthal anisotropy to continental dynamics, we can consider the geological history of the region. In the broadest of strokes, we note that the western U.S. has been tectonically active since the late Mesozoic, from the Laramide orogeny to the ongoing subduction-related orogenesis in the Cascades and extension in the Basin and Range. A relatively thinner lithosphere in the west likely plays a role in suggested sce-

narios where active mantle flow affects lithospheric deformation beneath the Basin and Range, the Colorado plateau and the Rockies (e.g. Savage and Sheehan, 2000; Karlstrom et al., 2012). Likewise, mantle flow itself may have eroded part of the lithosphere and caused thinning and extension at the Basin and Range (e.g. Lekić and Fischer, 2014). A thinner lithosphere relative to the cratonic eastern U.S. also implies a reduced role of possible shallow, frozen in anisotropy (e.g. Silver, 1996), and perhaps a more readily understandable link between asthenospheric flow and SWS.

The area through the central U.S. to the west of the Appalachian mountains is within the extent of the North American Craton, which is part of the oldest lithosphere on Earth that had been stable for over 1.7 Ga (e.g. Hoffman, 1989). The lithospheric root beneath the craton extends to over 200 km depth (e.g. Gung et al., 2003; Steinberger and Becker, 2016), and is suggested to have higher viscosity than the surrounding mantle (e.g. Lenardic and Moresi, 1999). Beneath the central U.S., the oldest part of the cratonic region is stable since the Archean, and may preserve relatively larger degrees of shallow, frozen-in anisotropy. On the other hand, the cratonic root may divert upper mantle flow, perturbing flow at the craton's edge and inducing counter flow beneath it, which could possibly strengthen regional lithosphere-

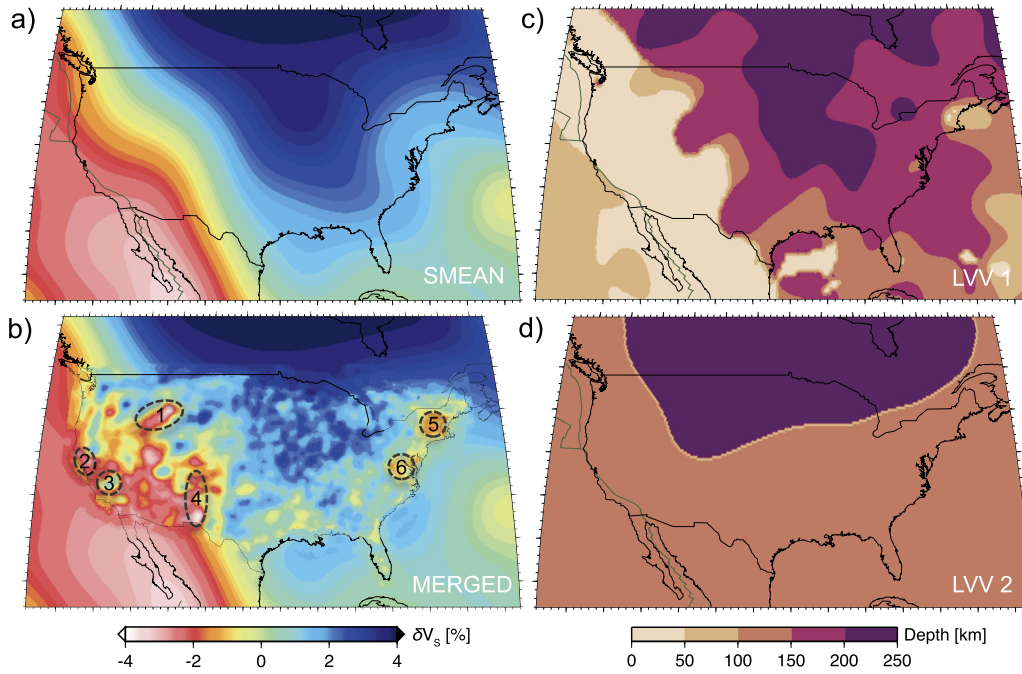


Fig. 2. Tomography (a and b) and lithospheric thickness (c and d) models. Colors in a) and b) indicate S wave velocity anomalies (δV_s) for the SMEAN (Becker and Boschi, 2002) and MERGED (cf. Schmandt and Lin, 2014) tomography models, respectively, at 200 km depth. In plot b), the outlined features are upper mantle anomalies that are discussed in the result section, they are: 1). Yellowstone and Snake River Plain, 2). Salton Trough, 3). northern Great Valley, 4). Rio Grande Rift, 5). New England, and 6) central Appalachian. Colors in c) and d) show the inferred depth of the lithosphere in viscosity models LVV1 and LVV2, respectively.

asthenosphere coupling (e.g. Silver, 1996; Fouch et al., 2000). This phenomenon is likely important for understanding the details of upper mantle flow dynamics and the origin of azimuthal anisotropy beneath the eastern U.S., which sits atop the cratonic boundary and edge.

Tectonic features in the eastern U.S. include the Proterozoic rifting and Paleozoic compressional orogenic events, followed by extensional events in the Mesozoic. Based on SWS splitting and modeling, Fouch et al. (2000) suggested that the observed anisotropy reveals the combined effect from the lithospheric and sublithospheric anisotropy in this region. Small-scale upper mantle density variations and lithospheric thickness variations exist in this region (Fig. 2) and might cause perturbations in anisotropy as well. For example, the northern Appalachian upwelling that can be inferred from slow seismic tomography anomalies (Schmandt and Lin, 2014) might relate to the Great Meteor hot spot track, and possibly indicate convection on relatively small scales in the surrounding mantle (e.g. Schmandt and Lin, 2014; Levin et al., 2018). Lithospheric thickness appears to decrease rapidly from the plateau to the east of the Appalachian, and is suggested to relate to lithospheric weakness from Eocene delamination (e.g. Mazza et al., 2014).

Convective flow models should be able to predict the current sublithospheric LPO to match the SWS observations if the models capture the major contributors that affect the present day upper mantle strain (e.g. Long and Becker, 2010). Given the extensive tectonic activity and prior sampling, much of the geodynamic SWS modeling previously focused on the western U.S. For example, Silver and Holt (2002) jointly interpreted splitting and GPS observations to infer eastward mantle flow. Becker et al. (2006b) computed LPO from mantle flow modeling, and showed that SWS outside the Basin and Range domain could be fit well with relatively simple flow models as long as a downwelling associated with the Farallon slab was included. More recently, Zhou et al. (2018) computed anisotropy from more complex models with lateral viscosity variations (LVVs) and were able to reproduce the circular pattern discussed by Zandt and Humphreys (2008).

Given the long geological history of the North American plate, we expect that the lithosphere-asthenosphere system will reflect different contributions to anisotropy. Based on joint surface wave and SWS analysis, Yuan and Romanowicz (2010) suggested layering with various lithospheric azimuthal anisotropy orientations beneath North America, and many authors have made the case that variations in SWS fast orientations with back-azimuth are best explained by a significant lithospheric anisotropy source (Silver, 1996; Savage, 1999).

Here, we seek to address azimuthal anisotropy underneath the U.S., explore which role small-scale lateral variations in density and viscosity play for predictions of asthenospheric anisotropy, and then return to the question of lithospheric anisotropy.

2. Methods

2.1. Mantle flow modeling

This study broadly follows the approach of Becker et al. (2006b) and Miller and Becker (2012). Under the Boussinesq and infinite Prandtl number approximations, the conservation equations for mass and momentum for mantle flow are given by

$$\begin{aligned} \nabla \cdot u &= 0, \\ -\nabla p + \nabla \cdot \eta(\nabla u + \nabla^T u) - \delta \rho g \hat{e}_r &= 0. \end{aligned}$$

Here, u is the velocity vector, p is the dynamic pressure, η is the viscosity, $\delta \rho$ is the density anomaly, g is the gravitational acceleration and \hat{e}_r is the radial unit vector. We solve the conservation equation using the finite element software CitcomS (Zhong et al., 2000) in a 3-D spherical domain. The surface boundary condition of most of our models are prescribed plate motions in the no-net-rotation (NNR) reference frame (NNR-NUVEL-1, by Argus and Gordon, 1991). The mechanical boundary condition at the core-mantle boundary is free-slip. Therefore, the absolute reference frame of the plate motions is irrelevant for relative velocities, and hence mantle flow predicted anisotropy.

Density variations outside continental cratons are assumed to be purely thermal and scaled from seismic tomography anomalies $\ln v_s$ with a simplified scaling of $R = \frac{d \ln \rho}{d \ln v_s}$. To ensure that the system is dynamically consistent, the resulting vigor of density-driven flow is adjusted via R such that when the same density variation is used in a model with free-slip surface boundary conditions, the same RMS surface velocity as for prescribed absolute plate motion (APM) results. The resulting $R = 0.24$ is in line with prior work (e.g. Miller and Becker, 2012). Inputs for the density variations come from two models: SMEAN is a composite, global S-wave tomography model (Becker and Boschi, 2002) used for reference (Fig. 2a). In order to capture the possible effect of small scale density anomalies beneath the U.S., we merge the regional tomography model of Schmandt and Lin (2014) with SMEAN to obtain MERGED where the edges of the embedded high resolution region are smoothed (Fig. 2b).

Within cratons, where we expect compositional anomalies (e.g. Jordan, 1978; Forte and Perry, 2000), we assume the lithosphere to be neutrally buoyant by setting craton-related seismic velocity anomalies to zero. The depth of the cratonic root is suggested to be ~200–250 km, for example by Yuan and Romanowicz (2010) and Gung et al. (2003), and geodynamic inversions (Forte and Perry, 2000). Since the tomography models we use show fast velocity anomalies that extend to ~300 km beneath the North American Craton, we use 300 km depth as the extent of the neutrally buoyant zone, for simplicity. The viscosity of the cratonic root is important in maintaining its long term stability. Convection modeling suggests it to be 100 to 1000 times more viscous than the ambient mantle (e.g. Lenardic and Moresi, 1999). Here we assume it to be 10 times more viscous than the continental lithosphere, which is 500 times the regular asthenosphere.

Both radial and lateral viscosity variations are considered. The viscosity model is built upon a three layered radial viscosity structure (RVV). The viscosity of each of the 0–100 km, 100–660 km, and 660–2891 km layers is 150, 1, and 60 times the reference value. For the 100–660 km depth range, a temperature dependent lateral viscosity variation (LVV) is applied to the three layered RVV structure, and the viscosity is given by equation: $\eta = \eta_0 \exp E(T - T_{ref})$. In this equation η_0 is from the RVV structure, E scales the effect of temperature dependence with a value of 7, T is the non-dimensional temperature at each point inferred from the tomography models, and T_{ref} is the non-dimensional reference temperature that equals to 0.5. In the upper 300 km, η is then multiplied by a structure dependent viscosity factor to account for the LVVs.

The viscosity factor at each of the plate boundaries, the oceanic and continental lithosphere, cratonic keels and oceanic asthenosphere is 0.01, 1, 50, 500, 0.01, respectively (cf. Miller and Becker, 2012). Focusing on continental keels underneath the U.S., we test two viscosity structures, models LVV1 and LVV2. The cratonic keel geometry of LVV1 is inferred from global tomography using the approach of Steinberger and Becker (2016) and the model SL2013 (Schaeffer and Lebedev, 2013). In LVV1, the minimum lithospheric thickness is 50 km in both continental and oceanic regions (Fig. 2c). LVV2 is taken from the reference craton model of Miller and Becker (2012) where keel geometry is simpler, and keel depth constant at 300 km (Fig. 2d).

2.2. Asthenospheric and lithospheric anisotropy modeling

Based on the mantle circulation models, we then use particle tracking and the D-Rex mineral physics approximation (Kaminski et al., 2004) to compute LPO as the tracers are advected until a logarithmic saturation strain of 0.75 is reached (Becker et al., 2006b; Miller and Becker, 2012). We assume that mantle circulation is stationary over the few Myr that it takes to achieve this strain (cf.

Becker et al., 2003, 2006a). Depth-dependent single crystal elasticity constants and Voigt averaging are then used to determine the elasticity tensor \mathbf{C} at 25 km spaced locations underneath each of the stations where SWS is measured.

While SKS splitting is well known to not linearly average over \mathbf{C} along the path, such differences are generally limited as long as anisotropy does not vary strongly with depth (e.g. Becker et al., 2012). We conducted tests using the full-waveform approach of Becker et al. (2006b) and found that regionally, details of the SWS predictions were affected. However, our overall conclusions regarding the flow model predictions would be the same.

Here, we therefore mainly consider the simplified, depth-averaged tensor approach, computing an average for the 25 to 375 km depth range, but we revisit a two layer case below. Under the tensor-averaging assumption, the Christoffel equation is then solved for the equivalent SWS delay times and fast azimuths using a back-azimuthal average.

Upon having predicted the inferred LPO anisotropy caused by mantle flow in the asthenosphere, we compare it with the SWS observation and compute the absolute angular misfit, $\Delta\alpha$, between the two ($\Delta\alpha \in [0^\circ, 90^\circ]$) for a range of flow models. Given the relatively poor overall fit for the study area of those predictions (Fig. 4 to 7) compared to earlier work (e.g. Miller and Becker, 2012), we also explore the possible contributions of the lithosphere more extensively. For this, we assume that there are two anisotropy layers, and the bottom layer is fixed to the flow model predicted anisotropy, which represents the depth averaged asthenospheric anisotropy. Then we invert for the best-fit “lithospheric complement” based on a parameter space exploration and Silver and Savage’s (1994) approach, and find the fast azimuth and delay time of the top layer anisotropy that, results in the best match to the back-azimuthally distributed SWS observations at each station.

3. Results

3.1. SWS alignment with absolute plate motions

Assuming that plate motions at the surface in some absolute reference frame (APM) are reflective of the orientation of shear between the lithosphere and mantle, APM alignment is a first order test for the origin of anisotropy (Silver, 1996). The SWS fast orientation beneath the U.S. are indeed found to be generally aligned with plate motion directions (e.g. Hongsresawat et al., 2015). Fig. 3 substantiates earlier analyses using our denser SWS dataset by comparing it with APM in the NNR reference frame (Argus and Gordon, 1991), and the spreading-aligned reference frame (Becker et al., 2015).

On a plate scale, SWS fast axes have NE-SW orientations similar to the NNR APM orientation of North America, especially in the western U.S. (Fig. 3a), leading to a plate-scale mean misfit of $\langle \Delta\alpha \rangle \approx 30^\circ$. The spreading-aligned APM is more similar to the SWS fast orientations and $\langle \Delta\alpha \rangle$ is further reduced by $\sim 5^\circ$ (Fig. 3b). While misfit values thus depend on different APM reference frames (e.g. Becker et al., 2015), similar local misfit fluctuations are observed, and those may be related to mantle flow deviating from implied APM shear. For example, in the southeastern Rockies (Fig. 3), the large angular misfit might relate to local lithospheric thickness variations (Refayee et al., 2014; Hongsresawat et al., 2015). Another significant misfit is found at the eastern U.S. and the southern Appalachian Mountains (Fig. 3), where anisotropy possibly contains a lithospheric frozen-in component (e.g. Levin et al., 2018; Long et al., 2016).

Table 1

Summary of the main information of all flow models discussed in this paper, through Model 1 to 11. Column 2 and 3 list the corresponding viscosity structure and density variation model of each flow model. Column 4 lists the average angular misfit between model predicted anisotropy and SWS observation. The surface boundary condition is prescribed APM for all flow models.

| Model number | Viscosity structures | Density variations ($\delta\rho$) | Average misfit ($^\circ$) |
|--------------|---|-------------------------------------|-----------------------------|
| 1 | no LVVs | no $\delta\rho$ | 44.6 $^\circ$ |
| 2 | cratons and plate boundaries in LVV1 | no $\delta\rho$ | 45.0 $^\circ$ |
| 3 | cratons, plate boundaries and oceanic asthenosphere in LVV1 | no $\delta\rho$ | 35.5 $^\circ$ |
| 4 | cratons and plate boundaries in LVV1 | SMEAN | 32.5 $^\circ$ |
| 5 | cratons and plate boundaries in LVV1 | MERGED | 38.2 $^\circ$ |
| 6 | no LVVs | SMEAN | 49.9 $^\circ$ |
| 7 | all structures in LVV1 | SMEAN | 40.5 $^\circ$ |
| 8 | all structures in LVV2 | SMEAN | 40.1 $^\circ$ |
| 9 | no LVVs | MERGED | 45.1 $^\circ$ |
| 10 | all structures in LVV1 | MERGED | 41.8 $^\circ$ |
| 11 | all structures in LVV2 | MERGED | 40.9 $^\circ$ |

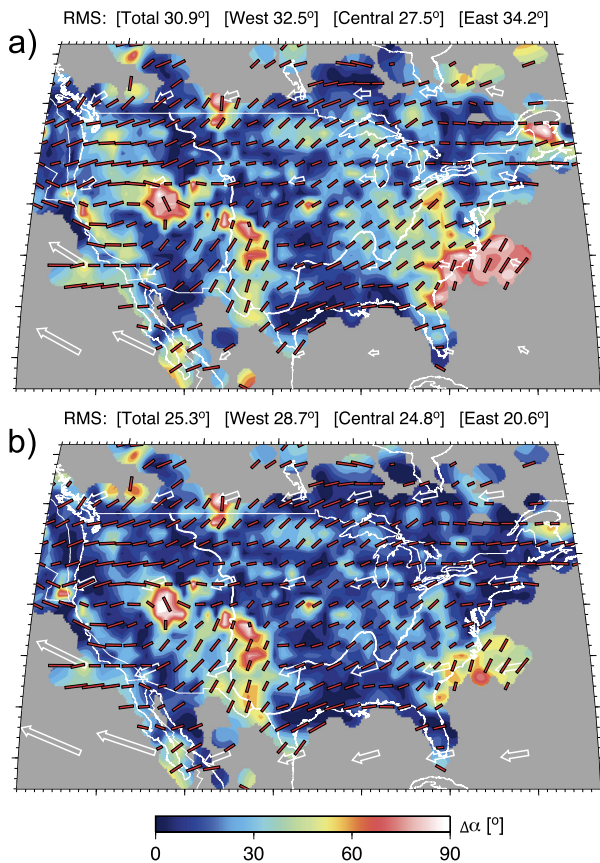


Fig. 3. Absolute angular misfit ($\Delta\alpha$) between *SKS* splits and absolute plate motion (APM) orientations in the no-net-rotation (NNR) reference frame of Argus and Gordon (1991) (a), and in the spreading-aligned reference frame of Becker et al. (2015) (b). $2^\circ \times 2^\circ$ grid averaged *SKS* splits (based on Fig. 1b) are shown by red sticks. APM motions are indicated by white, open vectors. Background color indicates the value of $\Delta\alpha$, and title shows the map-wide and regional means of $\Delta\alpha$ for the sub domains indicated by heavy white lines, ($\Delta\alpha$).

3.2. Flow model predictions for SWS

We now test the role of asthenospheric convection other than APM shearing by predicting anisotropy from the sublithospheric flow that is driven by plate motion alone, or in addition by density variations. We investigate the effect of viscosity variations caused by cratons, a weak oceanic asthenosphere layer, and plate boundary weak zones. For each flow model, we explore the flow itself, and compute the misfit between predicted and observed anisotropy, $\Delta\alpha$ (Table 1). We find it helpful to visualize the ef-

fect of shearing in flow models by plotting the vector difference \vec{v}_{shear} between the horizontal flow velocities at the surface $\vec{v}_{surface}$ and at a typical, 200 km depth \vec{v}_{200km} with

$$\vec{v}_{shear} = \vec{v}_{200km} - \vec{v}_{surface},$$

as such differential velocities can be a rough proxy for LPO alignment.

3.2.1. The effect of plate motion induced circulation with LVVs

Our starting Model 1 only has radial viscosity variations and is purely driven by prescribed plate motions. Given the effects of geometry and return flow, we expect that the induced asthenospheric shearing will be different from the APM model of Fig. 3 even for this simple circulation model (e.g. Long and Becker, 2010), and this is indeed the case.

Fig. 4a shows that beneath the western and central U.S., the direction of \vec{v}_{200km} deviates from the plate motion direction due to the flow perturbation at the Pacific-North America plate boundary. The flow direction is to the W to SW and the shear direction forms an 110° to 150° angle with the plate motion in this region. While details depend on the viscosity structure (cf. Becker et al., 2006b), this plate boundary flow perturbation extends almost throughout half the continent. In the Eastern U.S., sublithospheric Couette flow (Fig. 5a) is more in line with APM, such that shear is roughly into the opposite direction (Fig. 4a). The mis-alignment of shear and plate motion vectors is subdued in the eastern U.S. but still of order 20° to 30° .

Since there are no small-scale flow perturbation or abrupt changes in viscosity, the orientation of differential velocities of Fig. 4a are representative of the predicted anisotropy (Fig. 4b). W-E oriented predicted fast axes fit well with the SWS observation onshore in NW U.S. However, there are large misfits with regions of consistent $\sim 90^\circ$ misalignment such as the in the southern Rockies. The overall match between SWS and predictions is very poor at $\langle\Delta\alpha\rangle \approx 45^\circ$ (which is the expectation for random). This indicates that plate-induced shear flow without density anomalies is actually a much worse model in this case compared to the APM hypothesis of Fig. 3.

Based on Model 1, Model 2 adds in weak plate boundaries and strong cratonic keels from viscosity model LVV1. Comparing Models 1 and 2, changes in horizontal flow mainly occur beneath and around the craton (Figs. 4a and c). The spatial extent of this change is shown in the differential flow velocity profile in Fig. 5d. Due to its high viscosity, the craton maintains and enhances plate-like motion down to ~ 300 km depth, as shown in Fig. 4c, and transfers it to the sublithospheric mantle. The craton also causes minor flow perturbations in the radial direction at the lithospheric thickness discontinuities beneath the Colorado Plateau (Fig. 5d). However, the directional change in flow introduced by the keel is overall

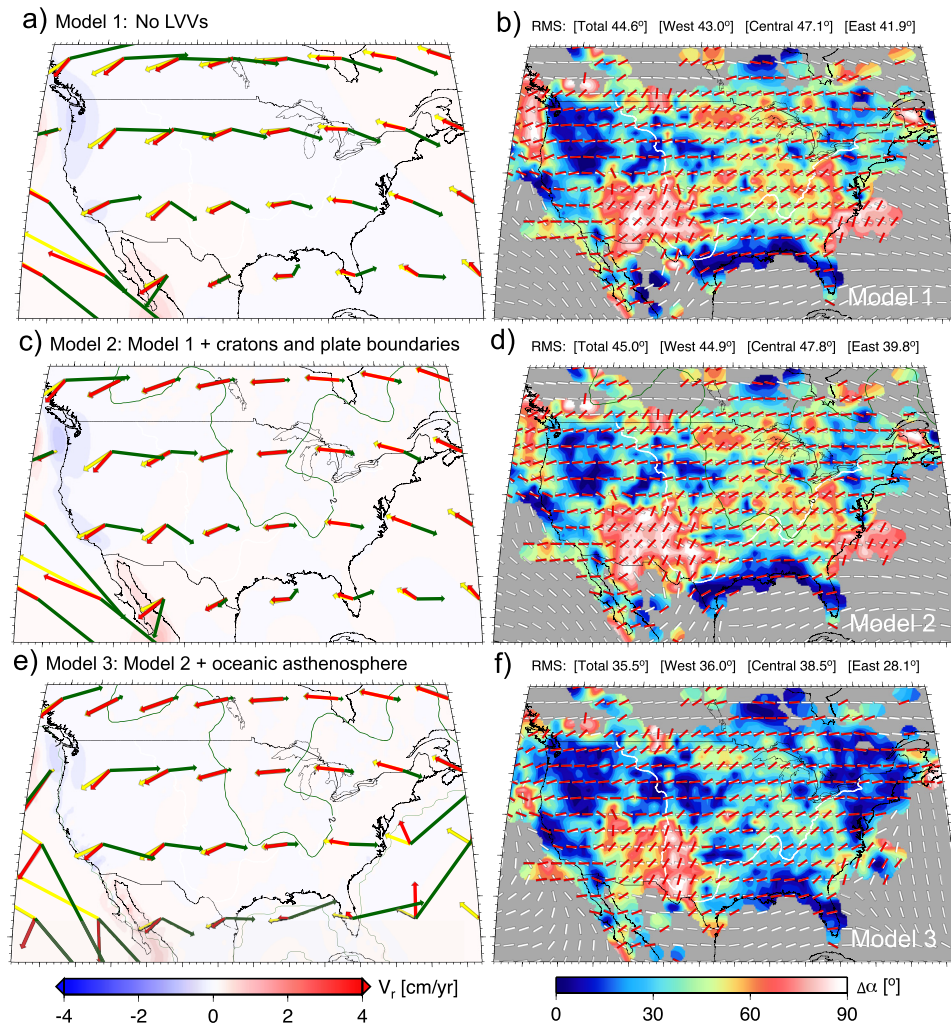


Fig. 4. Upper mantle flow (a, c, and e) and the resulting angular misfit ($\Delta\alpha$) between *SKS* splits and flow-model predicted anisotropy (b, d, and f) of Models 1 (plate-induced shear, a and b), 2 (added cratons and weak zones, c and d), and 3 (added oceanic weak asthenosphere, e and f). In plot a), c), and e), radial flow is shown in background coloring (upwelling positive); surface velocities, flow at 200 km depth, and their vector difference (amplified by 5) are indicated by yellow, red and green vectors, respectively. In plot b), d), and f), $\Delta\alpha$ is shown in the background; SWS observed and flow model predicted SWS fast orientations depicted by red and white vectors, respectively. Title for b), d), and f) shows mean angular misfits as in Fig. 2.

small, such that the anisotropy predictions of Models 1 and 2 are fairly similar (Figs. 4b and d). The weak plate boundary effect of Model 2 changes the flow and shear direction beneath the Juan de Fuca Plate, for example, slightly reducing $\Delta\alpha$ there (Fig. 4d).

Model 3 adds in a 200 km thick oceanic asthenosphere that is 100 times weaker than the ambient mantle compared to Model 2 (cf. Becker, 2017). Comparing the flow fields in Models 2 and 3, we see significant differences in flow pattern beneath the oceanic plates and adjacent areas (Figs. 4c and e). Differential velocities, \bar{v}_{200km} , and the APM within the oceanic region are nearly parallel in Model 2 (Fig. 4c), while in Model 3 they are perpendicular within the Pacific and form 40° to 60° angles within the Atlantic domain (Fig. 4e). The flow modification leads to a rotation in predicted anisotropy orientations from NW-SE in Model 2 to W-E in Model 3 (Figs. 4b and d).

Angular misfits $\Delta\alpha$ in Model 3 are reduced to $< 10^\circ$ in parts of the western and eastern U.S. (Fig. 4f). We see misfit reduction relative to Model 2 result (Fig. 4d) through most of the study area. Here, the weak sub-oceanic asthenosphere causes flow directional change to become more APM parallel than Model 2 through the south central and south eastern U.S. This effect, though small, can be seen from the change in shear direction and magnitude. At greater depth the flow changes to westward, so the depth-averaged

shear vector and predicted fast axes orient approximately W-E instead of parallel to the plate motion. Overall, the weak asthenosphere in plate-driven flow models accommodates the lithospheric shear beneath the Pacific plate, slows down the westward sublithospheric flow motion beneath the U.S., and amplifies return flow at 400 km depth (Figs. 5c and e). The misfit is overall reduced to $\langle \Delta\alpha \rangle \approx 36^\circ$ for Model 3. These tests suggest that a sub-oceanic viscosity reduction, as a much larger-scale feature compared to plate boundaries and continental cratons, can have a major control over the plate-driven shear (cf. Conrad and Lithgow-Bertelloni, 2006).

3.2.2. The effect of density driven flow

We next investigate the effect of density-driven flow by adding anomalies inferred from SMEAN and MERGED tomography models to Model 2, resulting in Models 4 and 5, respectively. The direction of \bar{v}_{200km} in Model 4 changes nearly 180° from the western to central U.S. (Fig. 6a) relative to Model 2, also clearly seen in the flow profile of Fig. 6e. This flow patterns results from an upwelling underneath the western U.S. and a lower-mantle, Farallon-related slab sinker anomaly. Those were earlier shown to lead to strong, APM opposite counter flow underneath the western half of the U.S. (e.g. Becker et al., 2006b), and are here seen to be further modulated by the cratonic keel.

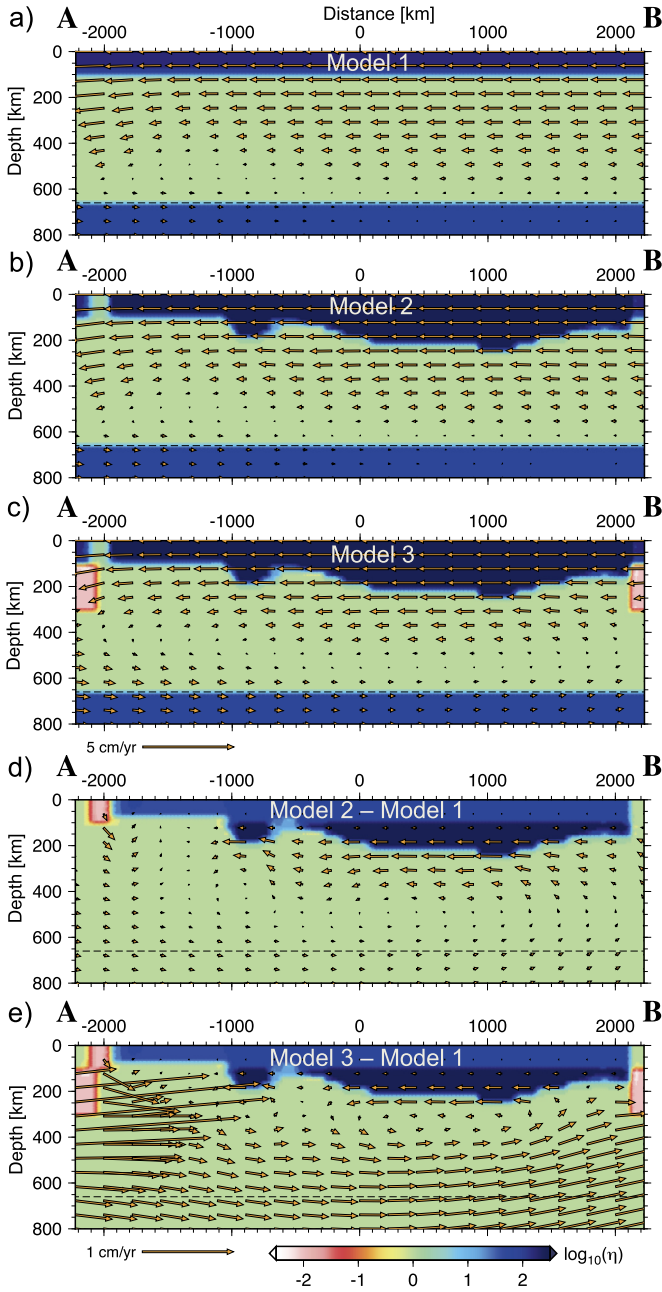


Fig. 5. Cross-section of mantle flow for Models 1 (a), 2 (b), and 3 (c) along the profile shown in Fig. 1a. Background color shows the decadic logarithm of the upper mantle normalized viscosity, and orange vectors show flow velocity with the length scale shown beneath the bottom left corner of plot c). Sub-plots d) and e) show the differences in flow field and viscosity between Models 1 and 2 (d), and between Models 1 and 3 (e). Length scale of the differential flow vectors is shown beneath plot e).

Density anomalies from SMEAN as incorporated in Model 4 result in shear and predicted anisotropy fast axes oriented W-E to WSW-ENE beneath the north western U.S. and west central U.S., W-E to WNW-ESE beneath the east central U.S. and north eastern U.S., and SW-NE beneath the south eastern U.S. (Figs. 6a and b). In these regions, the predicted anisotropy fits the SWS observation nearly as well as the APM model (Fig. 3), and the overall misfit is $\langle \Delta\alpha \rangle \approx 32^\circ$. This substantiates that a contribution of density-induced flow to plate-driven shear is needed for an appropriate prediction of LPO anisotropy, and hence a realistic mantle circulation estimate, as has been argued for global models (e.g. Behn et al., 2004; Becker et al., 2015).

The flow pattern and predicted anisotropy orientation in Model 5 based on MERGED are overall similar to Model 4 (Figs. 6c, d and Fig. 6f), but have, expectedly, more small-scale perturbations due to the higher resolution, regional tomography model of Schmandt and Lin (2014). Those features include the radial flow beneath Yellowstone and Snake River Plain (e.g. Savage and Sheehan, 2000), Salton Trough, northern Great Valley, Rio Grande Rift, New England and central Appalachian (Fig. 2b). Some of these smaller-scale flow structures inferred from MERGED affect the predicted anisotropy significantly. For example, beneath the northern Great Valley, which corresponds to a $\sim 5^\circ \times 5^\circ$ region with large $\Delta\alpha$ in Model 4, the dense structure that is suggested to be a lithospheric instability (Zandt et al., 2004) changes the predicted anisotropy orientation from nearly N-S in Model 4 to either SW-NE or NW-SE in Model 5, and results in a $\sim 45^\circ$ improvement in $\Delta\alpha$ values locally.

However, on balance, a degradation of the fit to SWS results on the scale of the whole U.S. is seen when the presumably better resolved MERGED tomography is used, with mean misfit increased to $\langle \Delta\alpha \rangle \approx 38^\circ$ (Fig. 6d). This means that asthenospheric flow is sensitively and diagnostically mapped into SWS predictions, but simply adding newer density models to existing flow computations at constant scaling does not provide a more consistent description of mantle dynamics. In fact, the opposite is true.

3.2.3. The effect of different LVV in density and plate-driven flow models

LVVs were seen to improve the fit of purely plate-driven flow to SWS observations (cf. Figs. 4b and f). Adding density-driven flow on large scales further improved the fit to observation to a level that is comparable to the APM model (Fig. 6b), but not for the smaller-scale anomalies of MERGED (Fig. 6d). We therefore explore the other major contribution to flow besides density, viscosity variations, further.

To complement the tests of Figs. 4 and 6 and focus on LVVs specifically, we explore six additional models (Figs. 7 and 8). For the tomography model SMEAN, we build a new reference, Model 6, by prescribing density variations to Model 1. We then build Models 7 and 8 by prescribing LVV models LVV1 and LVV2 to Model 6. Model 7 is different from Model 4 because it has the oceanic asthenosphere to allow for full investigation of the LVVs and also to help to distinguish the effect of the craton from the oceanic asthenosphere when comparing to Model 4. Similarly, for tomography model MERGED, we have Model 9 in which there are no LVVs, and Models 10 and 11 that use LVV1 and LVV2.

Without LVVs, the anisotropy predicted by Model 6 has W-E orientation beneath the north western U.S. and west central U.S. and fits the observed SWS regionally quite well (Fig. 7a). Other regions have very large angular misfits, raising the average to $\langle \Delta\alpha \rangle \approx 50^\circ$, worse than for pure plate-driven shear (Fig. 4b). Model 9 shows similar patterns (Fig. 7d), besides the southeastern edge of the western U.S., for example.

Comparing Model 7 to 6 (Figs. 7a and b) and Model 10 to 9 (Figs. 7d and e), we see that prescribing LVVs in flow models degrades the fit offshore the east coast, improves the fit between predicted and observed anisotropy in the central and eastern U.S., and largely modifies, although does not improve, the predicted anisotropy in the western U.S. (overall drop in $\langle \Delta\alpha \rangle$ is $\approx 6^\circ$ compared to no LVVs). Craton flow modification (Figs. 8b and e) affects regional misfits but does not lead to an overall improvement compared to the best flow model of Fig. 6b. Changing the viscosity structure to the LVV2 models leads to better coupled flow with the plate motion beneath the craton and thus changes the predicted anisotropy orientation in the northern part of the central and eastern U.S. (Figs. 7-c and f). LVV1 and LVV2 have different keel shapes (Figs. 2c and d) and deflect or lead the flow differently. Indeed,

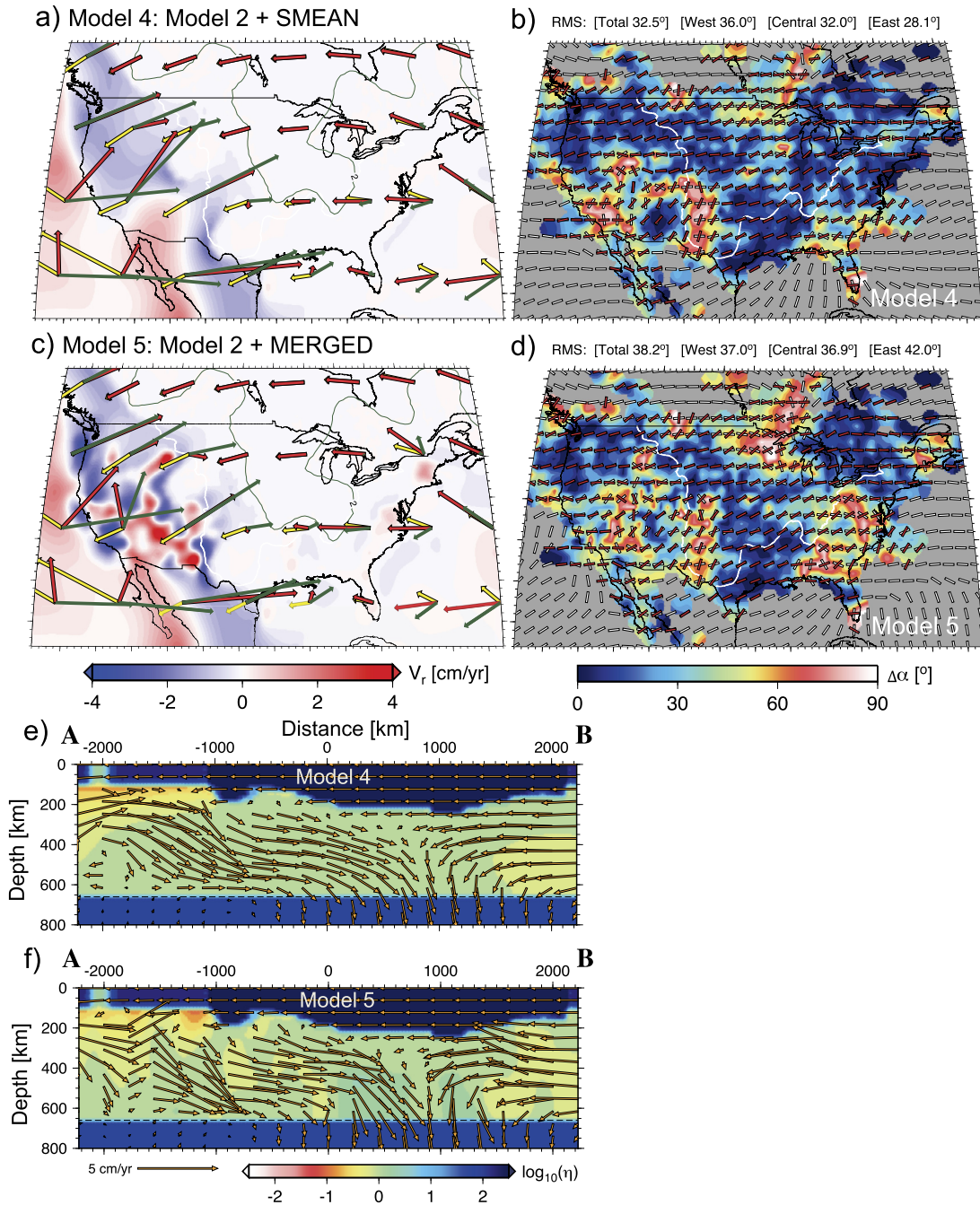


Fig. 6. Effect of density anomalies. Flow field at 200 km depth (a and c), the resulting $\Delta\alpha$ between SKS splits and flow predicted anisotropy (b and d) of Model 4 (SMEAN density driven flow, a and b) and 5 (MERGED density, c and d), and velocity and viscosity profiles for Models 4 (e) and 5 (f). Scale of velocity vector length is shown beneath plot f). See Fig. 4 and Fig. 5 for details.

comparing the regional mean misfits of Fig. 7b and c, as well as e and f, we can see changes particularly for the MERGED model. However, these effects of anisotropy modification are not overall beneficial, and the mean misfit values for models with the two viscosity structures are comparable.

Comparing flow profile residuals of the SMEAN flow models (Figs. 8b and c), they both show better coupled sublithospheric flow velocity beneath south central U.S. to the plate motion. The craton slows down the eastward flow beneath the western U.S., and speeds up the westward flow beneath the eastern U.S., relative to simpler viscosity models. For SMEAN, LVV1 causes more perturbations on the radial direction to the flow beneath it, while LVV2 mainly leads the sublithospheric flow horizontally. The MERGED

flow models have similar residual flow pattern overall, but see more variations in magnitude and direction upon adding the cratons (Figs. 8e and f), suggesting that the LVVs can amplify the density variation effects.

In summary, we find that the effects of different assumptions on asthenospheric density anomalies lead to the largest differences in predicted anisotropy. Yet, presumably higher resolution tomography does not improve the fit to SWS observations without additional model adjustments. Lateral viscosity variations help improve the fit when cratons and sub-oceanic viscosity reductions are introduced. Modifying the keel geometries between models LVV1 and LVV2 does improve the fit to SWS locally, but none of the modified LVV models we considered can make up for the degra-

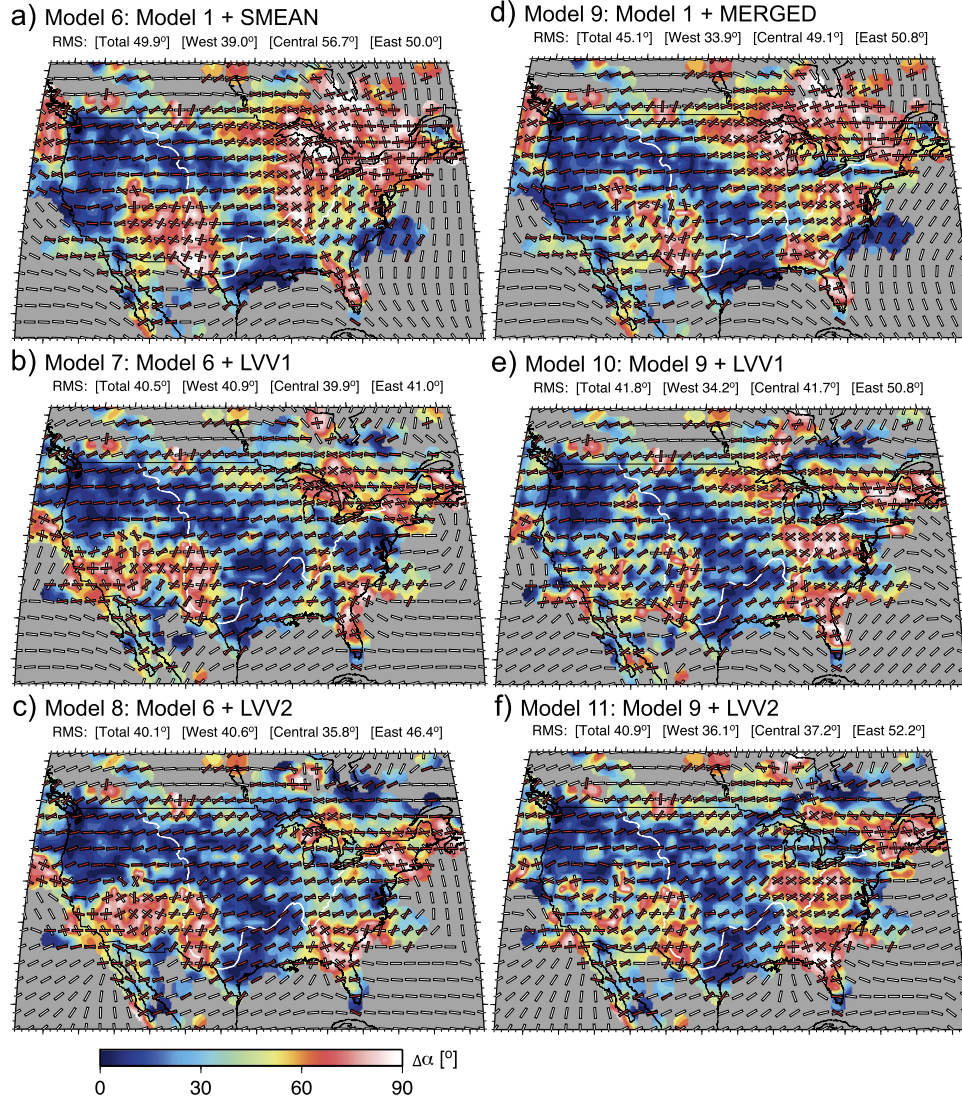


Fig. 7. Effect of lateral viscosity variations. $\Delta\alpha$ between SKS splits and flow-model predicted anisotropy of Models 6 (a), 7 (b), 8 (c), 9 (d), 10 (e), and 11 (f). See Fig. 4 for details.

duction of fit observed for MERGED compared to SMEAN density anomalies.

4. Discussion

4.1. Sensitivity of mantle flow modeling

We confirm that lateral viscosity variations can play an important role in controlling upper mantle flow underneath continental regions (e.g. Fouch et al., 2000; Miller and Becker, 2012). Plate-motion induced mantle-flow model predictions of SWS observations of azimuthal anisotropy are much improved when LVVs are added (Figs. 4b and f). This improvement is mainly due to the implementation of a strong cratonic keel and a weak oceanic asthenosphere which lead to enhancement and reduction of the coupling between plate motions and sublithospheric mantle, respectively (e.g. Conrad and Lithgow-Bertelloni, 2006; Becker, 2017). However, for purely plate-driven flow, the addition of a stiff craton does not cause significant regional flow deflection in lateral or radial directions, unlike what might be expected given experiments using simpler geometries (e.g. Fouch et al., 2000). Moreover, the fit to SWS of plate-driven flow is worse than the likely unphysical assumption of alignment with APM motions.

In models that also include the effect of mantle density anomalies for flow, in contrast, the craton amplifies the small-scale radial flow and causes more significant lateral deflection and strong downward deflection on scales that are relevant for regional anisotropy. In conjunction, the effects of density-driven flow and lateral viscosity variations are reflected in anisotropy, and SWS observations therefore do appear diagnostic of both density and viscosity anomalies on scales of 100s of km.

SWS and flow dynamic studies have, of course, long suggested the importance of density anomalies for North American plate dynamics, for example related to the Juan de Fuca and Farallon slabs (e.g. Becker et al., 2006b; Zandt and Humphreys, 2008), possible mantle drips (e.g. West et al., 2009) and mantle upwellings (e.g. Savage and Sheehan, 2000). Such anomalies should be better captured by the MERGED model based on regionally improved tomography, which makes it interesting that the addition of smaller-scale mantle structure actually leads to a worsening of the misfit between model predictions and azimuthal anisotropy observations (Figs. 6b and d). This was unexpected given prior successes of the general modeling approach.

Let us assume that structural models from seismology have in fact improved thanks to USArray, and that the most funda-

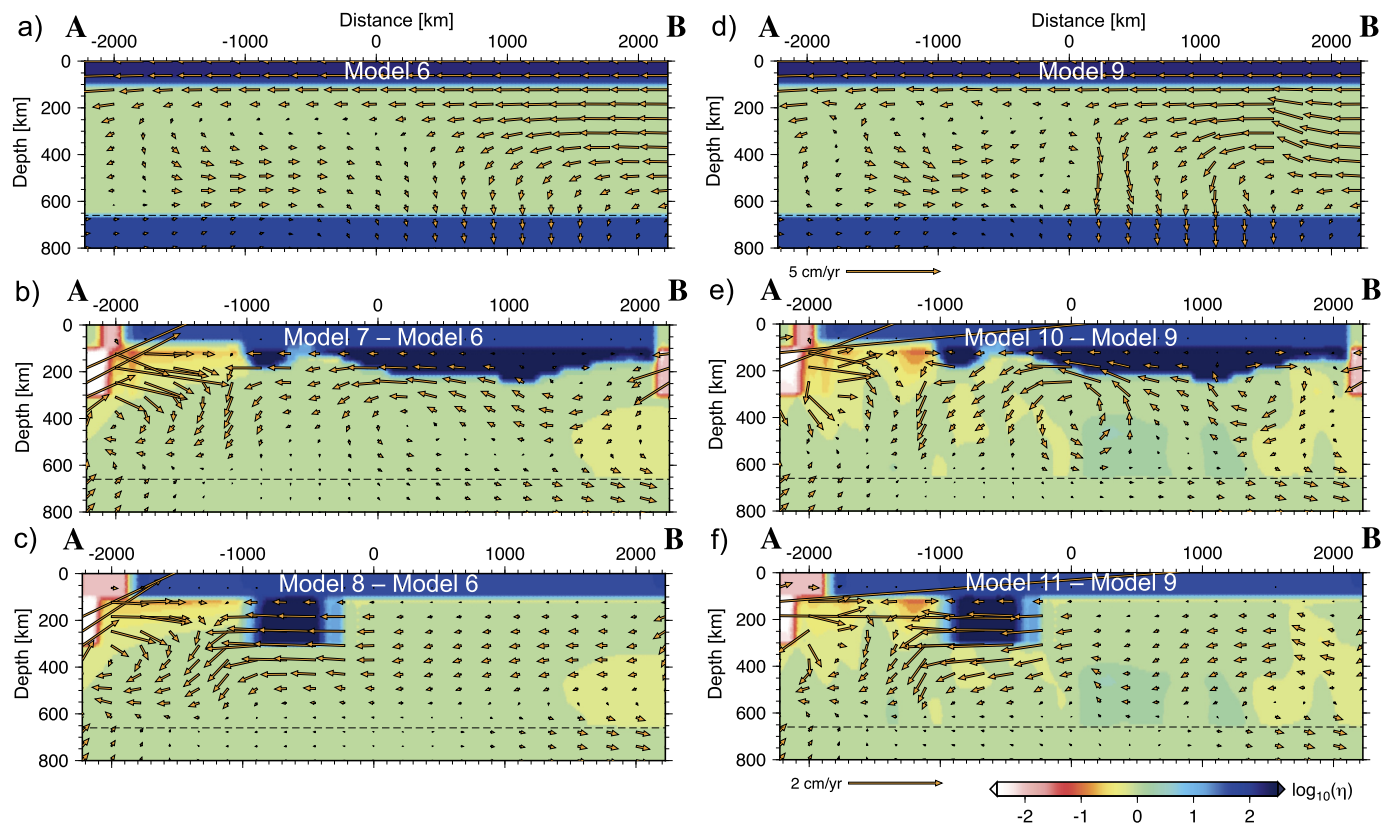


Fig. 8. Flow profiles of Models 6 (a) and 9 (f) with velocity vector length scale shown beneath plot f. Plots c, e, h) and j) show the differences in velocities and viscosity between Models 7 and 6 (c), Models 8 and 6 (e), Models 10 and 9 (h), and Models 11 and 9 (f). Differential velocity vector length scale is shown beneath plot j). See Fig. 5 for details.

mental assumptions for our approach hold, i.e. that upper mantle anisotropy is at least partially caused by LPO alignment under asthenospheric mantle flow, and that mantle flow can be estimated with mantle circulation models (e.g. Long and Becker, 2010). There are then several possible, not mutually exclusive, reasons for why our best circulation-based model is one that is based on plate-driven flow, the SMEAN large-scale mantle density anomalies, and simple LVVs.

First, given the sensitivity of LPO predictions to details of the LVVs, different keel structures, non-linear rheology, variations in volatile content, or additional compositional dependence of viscosity may all lead to lateral viscosity variations that counterbalance the detrimental effects of adding small-scale density structure of MERGED. A formal inversion for these variations is possible, but none of our forward tests (most not shown) trying different LVV structures have led to plate-scale improvement in mean misfit. Fig. 7 illustrates the sorts of variations in LPO predictions one might expect. These effects are in line with arguments about local effects, e.g. of drips and the like, but we leave the exploration of more complex mantle LVV models that could possibly reconcile the predictions for later. The general applicability of such optimized models will also be questionable should the LVVs not be based on some additional, general physical relationship not explored here.

Second, our scaling between seismic tomography and density anomalies might be wrong, and this is clearly the case in principle, given the highly simplified nature of our linear, depth-independent scaling. Besides temperature, other properties, especially compositional heterogeneity and anelasticity, can also affect seismic wave velocity (e.g. Forte and Perry, 2000; Cammarano et al., 2003). This might be of particular importance for the high resolution tomography model, which might demand lateral variations in the scaling factor. We expect that cratonic regions of the continental litho-

sphere may be neutrally buoyant (“isopycnic”, Jordan, 1978) which is why we corrected for this effect in a coarse fashion in our mantle flow models. The isopycnic assumption is not expected to be perfectly true at all depths, nor is the extent of cratons or the thickness of the lithosphere well constrained (e.g. Lekić and Fischer, 2014; Steinberger and Becker, 2016). We therefore cannot rule out that more sophisticated models including a wider range of compositional anomalies would lead to better predictions of LPO based anisotropy using the high resolution tomography models such as MERGED.

However, we conducted a range of tests where we varied the R scaling step wise from zero to its reference value, and found that the signal inherent in MERGED leads to a degradation of the fit compared to SMEAN as soon as the density effects are felt by mantle flow. This implies that compositional anomalies would have to cancel out much of the signal seen in MERGED compared to SMEAN to at least not degrade the fit. This is possible, but would also question the general interpretations of seismic tomography for regional tectonics.

Third, time-dependence of mantle convection, and in particular changes in plate motions, may complicate the interpretation of LPO based anisotropy even for the relatively short time-scales needed to saturate fabrics within the asthenosphere (e.g. Kaminski et al., 2004; Becker et al., 2006a). On global scales, Becker et al. (2003) showed that this effect was detectable, but seismological models did not allow determining which models were better within uncertainty.

Regionally, the story may be different, and Zhou et al. (2018) explored such effects for the western U.S. in detail. The authors pointed out the importance of the Juan de Fuca slab and a hot mantle anomaly beneath the western U.S. for the formation of the circular anisotropy beneath the Great Basin. However, the

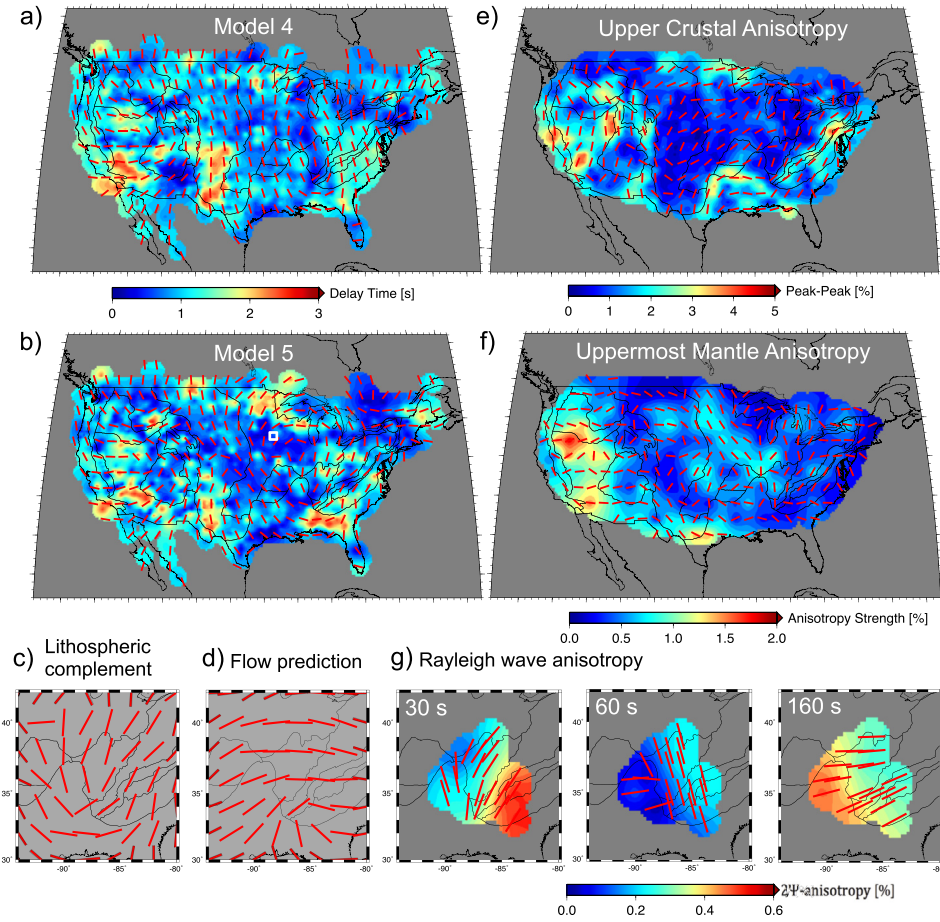


Fig. 9. Inferred lithospheric anisotropy resulting from matching Model 4 (a) and 5 (b) flow-predicted anisotropy to the SWS dataset. c) shows the Model 5 lithospheric anisotropy orientation within the white rectangular box in b), and d) shows the Model 5 flow predicted anisotropy within the same region. e) shows crustal anisotropy from Lin and Schmandt (2014). f) shows the uppermost mantle anisotropy from Buehler and Shearer (2017). g) shows regional Rayleigh wave anisotropy model from Deschamps et al. (2008), with each of the subplots showing different Rayleigh wave periods as noted on the upper left corner. In all plots, the red vector shows fast orientation. The background color shows the delay time in a) and b), shows the peak to peak amplitude in e), anisotropy magnitude in f), and shows 2ψ anisotropy magnitude in g).

anisotropy adjacent to that pattern was not well fit, implying similarly mixed results in terms of a comprehensive explanation of SWS observations.

There are thus at least three plausible reasons why a purely asthenospheric origin of anisotropy appears to be a moderately successful explanation of the large-scale SWS signal for the U.S. at best. In the remainder, we will instead assume, for the sake of argument, that our computations are in fact very good predictions of asthenospheric anisotropy, so good that we can ask about a missing lithospheric component needed to fit SWS observations.

4.2. The lithospheric complement

A lithospheric, frozen-in origin of anisotropy has long been discussed for the shallow oceanic lithosphere, as well as the bulk of the thicker and petrologically more heterogeneous continental lithosphere (e.g. Silver, 1996). Assuming that the difference between the SWS observations and flow predictions of LPO anisotropy arises entirely from the lithospheric component, we can augment a flow model with its corresponding lithospheric complement that would be needed to achieve a (near) perfect fit to SKS splitting.

Fig. 9 shows results for the lithospheric complements for the best performing LPO based on flow models, Model 4 (SMEAN) and 5 (MERGED). The lithospheric complement is found by fitting individual splits from Liu et al. (2014) with a two-layer model, in

which the bottom layer is fixed to the flow predicted anisotropy. The values of the apparent splitting parameters from the hypothetical two-layer anisotropy and the average of the SKS splits are similar (Fig. S1), with angular difference of $\Delta\alpha \lesssim 5^\circ$, which would be within the typical “error” of SWS estimates. For stations where the flow predicted anisotropy has similar orientation to the bottom layer from an independent two-layer inversion of SKS splits, the hypothetical lithospheric anisotropy is also similar to the top layer from the independent inversion. This suggests the validity of this approach for studying multi-layer anisotropy. Besides the two layer parameter space exploration approach, we also explore a simple method of matching SWS by inverting for the best-fit thickness and anisotropy orientation of a lithospheric layer that consists of frozen-in anisotropy represented by a single elastic tensor (supp. mat.). Using this method, the inferred lithospheric complement has similar orientation with our current approach, but the delay times are less realistic (Fig. S2). We leave the exploration of back-azimuthal dependence of SKS splitting for a future joint analysis with surface-wave depth-dependent anisotropy.

As Figs. 9a and b show, the patterns of the best fit lithospheric complement are fairly smooth over much of the study area. This might be expected from the spatial heterogeneity of SWS and seismic tomography, but implies that there could be a relation with a deterministic tectonic or convective process. The lithospheric complement is different for the two flow models in detail, but there are also consistent features. That said, the connection of the litho-

spheric complement's azimuthal alignment patterns to geological history is not immediately apparent, at least to us.

However, we can check if the features of the complement are at least consistent with other possibly related observations. To this end, we visually compare the complements with an azimuthal anisotropy model inferred from 16 s period Rayleigh waves by Lin and Schmandt (2014) (Fig. 9e). While mainly sensitive to the uppermost crust, the anisotropy orientations appear related to tectonic regions, such as the Great Basin, the Rockies and the Precambrian Rift Margin (Lin and Schmandt, 2014). Without going to details of the relationship between crustal anisotropy and tectonics, we note that there are fairly good correlations in orientations between our lithospheric complement and the crustal anisotropy along the west coast of the U.S., beneath the Columbia Plateau, the southern Basin and Range, south of the Colorado plateau, Texas and the southern Coastal Plain (Figs. 9a and b). Beneath the eastern U.S., Model 5's lithospheric complement matches the crustal model while Model 4's does not.

To expand this comparison to the uppermost mantle, we further compare the Model 5 lithospheric complement with the Pn anisotropy model by Buehler and Shearer (2017) (Figs. 9f). This model provides information beneath the Moho. In this model, the NE-SW oriented orogeny parallel anisotropy beneath the Appalachian mountain and east central U.S. only exist in the central region (Fig. 9f). In other regions of the eastern U.S., the anisotropy is E-W, which might relate to plate motion (Buehler and Shearer, 2017). If this is the case, we would expect orogeny parallel anisotropy at shallow depths, and more plate motion parallel anisotropy beneath. This is true when we look at the Model 5 results, where the flow model predicted anisotropy parallels the plate motion (Fig. 6d), and the lithospheric complement parallels the orogeny (Fig. 9b). Since the SKS splits have a more dominant orogeny parallel pattern compared to the uppermost mantle anisotropy, there might be a significant crustal contribution in the SWS observation at the eastern and east-central U.S., which partly explains the misfit we observed when comparing the flow predicted anisotropy to SWS in this region.

To investigate the anisotropy at different depths in the eastern and east-central U.S., we compare our lithospheric complement with the regional model by Deschamps et al. (2008) (Fig. 9g). The lithospheric complement of Model 5 (Fig. 9c) has similar patterns with the Rayleigh wave anisotropy at periods < 60 s, which approximately shows the lithosphere. The longer period (160 s) Rayleigh wave anisotropy, however, does not match the lithospheric complement, but matches the flow predicted anisotropy in the same region (Fig. 9d). This depth constraint of anisotropy further suggests that the actual lithospheric anisotropy is reasonably estimated by the lithospheric complement, and the lithosphere has notable contribution to the SWS observation, at least in the eastern and east-central U.S.

Good correlation between lithospheric complement and the lithospheric anisotropy, and between flow model prediction and the sublithospheric anisotropy in the eastern U.S. indicate the possibility that MERGED predicts the sublithospheric anisotropy better than SMEAN even if the asthenospheric LPO alone leads to a poor fit. This substantiates importance of understanding lithospheric anisotropy, and may help to resolve the connection between small-scale mantle structures and the upper mantle anisotropy formation and SWS observation.

New insights into continental dynamics may yet be revealed by modeling anisotropy due to mantle flow. However, the answer might at least regionally have to involve more detailed study of the lithosphere and longer-term geological history. Such future work should be especially promising once noise and ballistic surface wave inferences for crustal and mantle anisotropy are adequately incorporated.

5. Conclusions

Azimuthal anisotropy in the upper mantle as seen by shear wave splitting throughout the U.S. and offshore portions of the North American plate can be modeled by mantle circulation models. These models allow exploring the effect of density anomalies and viscosity variations within the asthenosphere, which strongly affect predictions when acting together. Large-scale flow models lead to misfits that are comparable to the absolute plate motion alignment hypothesis for the study region. This confirms the general validity of the approach, but smaller-scale density anomalies of modern, EarthScope era tomography degrade the fit, and none of the viscosity models we considered can make up for it. "Lithospheric complements" can be estimated from the best flow model based anisotropy, and those match independent estimates of crustal anisotropy. This indicates promising avenues forward, but much is still to be learned about the link between seismic anisotropy and mantle flow and continental dynamics.

Acknowledgements

WW and TWB were partially supported by NSF EAR-1460479. All figures were prepared with the Generic Mapping Tools. We thank B. Schmandt and F. Lin for sharing their tomography and crustal anisotropy models with us. We thank our collaborators, K. Liu and S. Gao, for sharing their SWS dataset with us. We also thank L. Fuchs and R. Porritt at the Geodynamics group at the Jackson School of Geosciences for help and discussions.

Appendix A. Supplementary material

Supplementary material related to this article can be found online at <https://doi.org/10.1016/j.epsl.2019.03.019>.

References

- Argus, D.F., Gordon, R.G., 1991. No-net-rotation model of current plate velocities incorporating plate motion model NUVEL-1. *Geophys. Res. Lett.* 18 (11), 2039–2042.
- Becker, T.W., 2017. Superweak asthenosphere in light of upper-mantle seismic anisotropy. *Geochem. Geophys. Geosyst.* 18, 1986–2003.
- Becker, T.W., Boschi, L., 2002. A comparison of tomographic and geodynamic mantle models. *Geochem. Geophys. Geosyst.* 3 (1).
- Becker, T.W., Chevrot, S., Schulte-Pelkum, V., Blackman, D.K., 2006a. Statistical properties of seismic anisotropy predicted by upper mantle geodynamic models. *J. Geophys. Res.* 111 (B8), B08309.
- Becker, T.W., Kellogg, J.B., Ekström, G., O'Connell, R.J., 2003. Comparison of azimuthal seismic anisotropy from surface waves and finite strain from global mantle-circulation models. *Geophys. J. Int.* 155 (2), 696–714.
- Becker, T.W., Lebedev, S., Long, M.D., 2012. On the relationship between azimuthal anisotropy from shear wave splitting and surface wave tomography. *J. Geophys. Res., Solid Earth* 117 (B1).
- Becker, T.W., Schaeffer, A.J., Lebedev, S., Conrad, C.P., 2015. Toward a generalized plate motion reference frame. *Geophys. Res. Lett.* 42 (9), 3188–3196.
- Becker, T.W., Schulte-Pelkum, V., Blackman, D.K., Kellogg, J.B., O'Connell, R.J., 2006b. Mantle flow under the western United States from shear wave splitting. *Earth Planet. Sci. Lett.* 247 (3–4), 235–251.
- Behn, M.D., Conrad, C.P., Silver, P.G., 2004. Detection of upper mantle flow associated with the African Superplume. *Earth Planet. Sci. Lett.* 224, 259–274.
- Bodmer, M., Toomey, D.R., Hooft, E.E., Braunmiller, J., 2015. Seismic anisotropy beneath the Juan de Fuca plate system: evidence for heterogeneous mantle flow. *Geology* 43.
- Buehler, J.S., Shearer, P.M., 2017. Uppermost mantle seismic velocity structure beneath USArray. *J. Geophys. Res., Solid Earth* 122 (1), 436–448.
- Cammarano, F., Goes, S., Vacher, P., Giardini, D., 2003. Inferring upper-mantle temperatures from seismic velocities. *Phys. Earth Planet. Inter.* 138 (3–4), 197–222.
- Conrad, C.P., Lithgow-Bertelloni, C., 2006. Influence of continental roots and asthenosphere on plate-mantle coupling. *Geophys. Res. Lett.* 33 (5), L05312.
- Deschamps, F., Lebedev, S., Meier, T., Trampert, J., 2008. Azimuthal anisotropy of Rayleigh-wave phase velocities in the east-central United States. *Geophys. J. Int.* 173 (3), 827–843.
- Forté, A.M., Perry, H.K., 2000. Geodynamic evidence for a chemically depleted continental tectosphere. *Science* 290 (5498), 1940–1944.

- Fouch, M.J., Fischer, K.M., Parmentier, E.M., Wyssession, M.E., Clarke, T.J., 2000. Shear wave splitting, continental keels, and patterns of mantle flow. *J. Geophys. Res., Solid Earth* 105 (B3), 6255–6275.
- Gung, Y., Panning, M., Romanowicz, B., 2003. Global anisotropy and the thickness of continents. *Nature* 422 (6933), 707–711.
- Hoffman, P.F., 1989. Speculations on Laurentia's first gigayear (2.0 to 1.0 Ga). *Geology* 17 (2), 135.
- Hongsresawat, S., Panning, M.P., Russo, R.M., Foster, D.A., Monteiller, V., Chevrot, S., 2015. USArray shear wave splitting shows seismic anisotropy from both lithosphere and asthenosphere. *Geology* 43 (8), 667–670.
- Jordan, T.H., 1978. Composition and development of the continental tectosphere. *Nature* 274 (5671), 544–548.
- Kaminski, E., Ribe, N.M., Browaeys, J.T., 2004. D-rex, a program for calculation of seismic anisotropy due to crystal lattice preferred orientation in the convective upper mantle. *Geophys. J. Int.* 158, 744–752.
- Karlstrom, K.E., Coblenz, D., Dueker, K., Ouimet, W., Kirby, E., Van Wijk, J., Schmandt, B., Kelley, S., Lazear, G., Crossey, L.J., Crow, R., Aslan, A., Darling, A., Aster, R., MacCarthy, J., Hansen, S.M., Stachnik, J., Stockli, D.F., Garcia, R.V., Hoffman, M., McKeon, R., Feldman, J., Heizler, M., Donahue, M.S., 2012. Mantle-driven dynamic uplift of the Rocky Mountains and Colorado Plateau and its surface response: toward a unified hypothesis. *Lithosphere* 4, 3–22.
- Lekić, V., Fischer, K.M., 2014. Contrasting lithospheric signatures across the western United States revealed by Sp receiver functions. *Earth Planet. Sci. Lett.* 402, 90–98.
- Lenardic, A., Moresi, L.-N., 1999. Some thoughts on the stability of cratonic lithosphere: effects of buoyancy and viscosity. *J. Geophys. Res., Solid Earth* 104 (B6), 12747–12758.
- Levin, V., Long, M.D., Skryzalin, P., Li, Y., López, I., 2018. Seismic evidence for a recently formed mantle upwelling beneath New England. *Geology* 46 (1), 87–90.
- Lin, F.-C., Schmandt, B., 2014. Upper crustal azimuthal anisotropy across the contiguous U.S. determined by Rayleigh wave ellipticity. *Geophys. Res. Lett.* 41 (23), 8301–8307.
- Liu, K.H., Elsheikh, A., Lemnifi, A., Purevsuren, U., Ray, M., Refayee, H., Yang, B.B., Yu, Y., Gao, S.S., 2014. A uniform database of teleseismic shear wave splitting measurements for the western and central United States. *Geochem. Geophys. Geosyst.* 15 (5), 2075–2085.
- Long, M.D., Becker, T.W., 2010. Mantle dynamics and seismic anisotropy. *Earth Planet. Sci. Lett.* 297 (3–4), 341–354.
- Long, M.D., Jackson, K.G., McNamara, J.F., 2016. SKS splitting beneath transportable array stations in eastern North America and the signature of past lithospheric deformation. *Geochem. Geophys. Geosyst.* 17 (1), 2–15.
- Lynner, C., Bodmer, M., 2017. Mantle flow along the eastern North American margin inferred from shear wave splitting. *Geology* 45 (10), 867–870.
- Mazza, S.E., Gazel, E., Johnson, E.A., Kunk, M.J., McAleer, R., Spotila, J.A., Bizimis, M., Coleman, D.S., 2014. Volcanoes of the passive margin: the youngest magmatic event in eastern North America. *Geology* 42 (6), 483–486.
- Miller, M.S., Becker, T.W., 2012. Mantle flow deflected by interactions between subducted slabs and cratonic keels. *Nat. Geosci.* 5 (10), 726–730.
- Ramsay, J., Kohler, M.D., Davis, P.M., Wang, X., Holt, W., Weeraratne, D.S., 2015. North America plate boundary offshore southern California. *Geophys. J. Int.* 207.
- Refayee, H.A., Yang, B.B., Liu, K.H., Gao, S.S., 2014. Mantle flow and lithosphere–asthenosphere coupling beneath the southwestern edge of the North American craton: constraints from shear-wave splitting measurements. *Earth Planet. Sci. Lett.* 402, 209–220.
- Savage, M.K., 1999. Seismic anisotropy and mantle deformation: what have we learned from shear wave splitting? *Rev. Geophys.* 37, 65–106.
- Savage, M.K., Sheehan, A.F., 2000. Seismic anisotropy and mantle flow from the Great Basin to the Great Plains, western United States. *J. Geophys. Res., Solid Earth* 105 (B6), 13715–13734.
- Schaeffer, A.J., Lebedev, S., 2013. Global shear speed structure of the upper mantle and transition zone. *Geophys. J. Int.* 194 (1), 417–449.
- Schmandt, B., Lin, F.-C., 2014. P and S wave tomography of the mantle beneath the United States. *Geophys. Res. Lett.* 41 (18), 6342–6349.
- Silver, P.G., 1996. Seismic anisotropy beneath the continents: probing the depths of geology. *Annu. Rev. Earth Planet. Sci.* 24, 385–432.
- Silver, P.G., Holt, W.E., 2002. The mantle flow field beneath Western North America. *Science* 295, 1054–1057.
- Silver, P.G., Savage, M.K., 1994. The interpretation of shear-wave splitting parameters in the presence of two anisotropic layers. *Geophys. J. Int.* 119 (3), 949–963.
- Steinberger, B., Becker, T.W., 2016. A comparison of lithospheric thickness models. *Tectonophysics*.
- West, J.D., Fouch, M.J., Roth, J.B., Elkins-Tanton, L.T., 2009. Vertical mantle flow associated with a lithospheric drip beneath the Great Basin. *Nat. Geosci.* 2 (6), 439–444.
- Yang, B.B., Liu, K.H., Dahm, H.H., Gao, S.S., 2016. A uniform database of teleseismic shear-wave splitting measurements for the Western and Central United States: December 2014 update. *Seismol. Res. Lett.* 87 (2A), 295–300.
- Yang, B.B., Liu, Y., Dahm, H., Liu, K.H., Gao, S.S., 2017. Seismic azimuthal anisotropy beneath the eastern United States and its geodynamic implications. *Geophys. Res. Lett.* 44 (6), 2670–2678.
- Yuan, H., Romanowicz, B., 2010. Lithospheric layering in the North American craton. *Nature* 466 (7310), 1063–1068.
- Zandt, G., Gilbert, H., Owens, T.J., Ducea, M., Saleeby, J., Jones, C.H., 2004. Active foundering of a continental arc root beneath the southern Sierra Nevada in California. *Nature* 431 (7004), 41–46.
- Zandt, G., Humphreys, E., 2008. Toroidal mantle flow through the western U.S. slab window. *Geology* 36 (4), 295.
- Zhong, S., Zuber, M.T., Moresi, L.N., Gurnis, M., 2000. Role of temperature-dependent viscosity and surface plates in spherical shell models of mantle convection. *J. Geophys. Res.* 105, 11063–11082.
- Zhou, Q., Hu, J., Liu, L., Chaparro, T., Stegman, D.R., Faccenda, M., 2018. Western U.S. seismic anisotropy revealing complex mantle dynamics. *Earth Planet. Sci. Lett.* 500, 156–167.